

CT-AGR: AUTOMATED ABNORMALITY-GUIDED REPORT GENERATION FROM 3D CHEST CT VOLUMES

Theo Di Piazza^{1,2}

¹CREATIS, INSA Lyon, University of Lyon 1, Villeurbanne, France

²Hôpitaux Civils de Lyon, Lyon, France

The rapid increase of computed tomography (CT) scans and their time-consuming manual analysis have created an urgent need for robust automated analysis techniques in clinical settings. These aim to assist radiologists and help them managing their growing workload. Existing methods typically generate entire reports directly from 3D CT images, without explicitly focusing on observed abnormalities. This unguided approach often results in repetitive content or incomplete reports, failing to prioritize anomaly-specific descriptions. We propose a new anomaly-guided report generation model, which first predicts abnormalities and then generates targeted descriptions for each. Evaluation on a public dataset demonstrates significant improvements in report quality and clinical relevance. We extend our work by conducting an ablation study to demonstrate its effectiveness.

1. INTRODUCTION

Three-dimensional Computed Tomography (3D CT) scans have emerged as indispensable tools in medical imaging [1], offering unparalleled insights into anatomical structures and pathological conditions. Given the rapidly increasing number of scans to analyze [2, 3, 4], the time-consuming nature of the task [5] and the important demand for specialized radiological expertise in numerous healthcare systems [6, 7], automating report generation has emerged as an active research area [8, 9, 10]. Whether dealing with 2D [11, 12] or 3D [13, 14] images, numerous deep learning methods have been introduced to support healthcare professionals in tasks such as anomaly classification [13, 15], detection [16, 17, 18], segmentation [19, 20, 21], and report generation [9, 10, 22, 23]. Indeed, the availability of public datasets for 2D radiology images [12, 11] has facilitated the development of such methods [22, 23, 24, 25, 26, 27]. Recently, CT2Rep [10] has been presented as the first 3D method for automated report generation, trained and evaluated on the public CT-RATE dataset [14]. The baseline, CT2Rep, uses an Encoder-Decoder model to generate reports directly from 3D CT scans. However, this end-to-end approach may lead to incomplete or partially incorrect report [6]. When composing a report [28], a radiologist aims to detect abnormalities and then provide descriptions for each identified abnormality. Inspired by the

radiologists' workflow, we propose a method that first predicts anomalies and then generates a specific sentence for each anomaly. Our contributions are as follows:

- We introduce a new abnormality-based sentence generation model that enhances chest 3D CT scan report generation performance, achievable with limited computational resources (single GPU, 24-hour training time).
- We leverage a pre-trained language model that we condition to generate a sentence for each abnormality.
- We evaluate the model on a public dataset and we enhance our findings with an ablation study to show the effectiveness of each module.

2. RELATED WORK

2.1. 2D Radiology report generation

Image captioning has emerged as a crucial task across diverse research domains [29, 30, 31, 32, 33]. This field has garnered significant attention in recent years in recent years [34, 35, 36], with applications in automated medical image reporting [37]. Early supervised methods for 2D radiology report generation [11, 12] primarily used Encoder-Decoder architectures [24, 25, 38]. The features of the input image are extracted using an encoder, either a CNN [39] or a Vision Transformer [40, 41]. These image-level features are then passed to a decoder, corresponding to a RNN [42] or Transformer Decoder [23, 26], which predicts the corresponding report. More recent methods introduce relational memory [23], pathology tags [43], or reinforcement learning [44] to improve the quality of generated reports. However, these methods generate the entire report only from the radiology image. Given the complexity and the inherent variability in radiological findings, these methods tend to produce incomplete or partially incorrect reports [6]. Guided methods were then introduced to facilitate report generation [45, 46]. Descriptive sentences specific to identified regions or predicted abnormalities can be generated through the integration of an anatomical region detection or abnormality classification module [22].

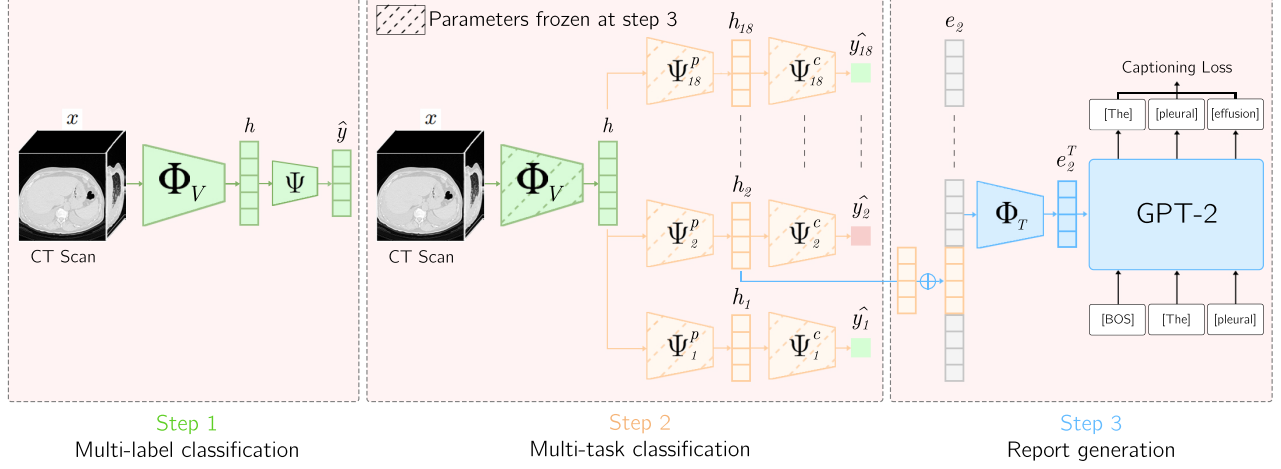


Fig. 1: Overview of the method. **Step 1.** The input volume x is passed through a visual extractor Φ_V (either CT-ViT [47] or CT-Net [13]) to extract an embedding h . h is then given to classification head Ψ which predicts the logit vector \hat{y} . **Step 2.** h is fed into 18 projection heads ($\Psi_i^p, i \in \{1, \dots, 18\}$) followed by small classification heads ($\Psi_i^c, i \in \{1, \dots, 18\}$), one for each label. This second step enables to obtain an embedding h_i (and then e_i) specific to each label. **Step 3.** If a label indexed by i is predicted as abnormal by its corresponding classification head Ψ_i^c , the associated embedding e_i is given to a lightweight MLP $\Phi_T(e_i)$ to obtain e_i^T . An abnormality-specific description is generated from a pre-trained GPT-2 using e_i^T .

2.2. 3D Radiology report generation

New challenges arise with 3D imaging [48, 49] and especially computed tomography (CT). Compared to 2D images, this modality of data introduces new difficulties due to the limited availability of public datasets [10] in this field and the significant computational resources needed [48, 49]. Abnormality detection [18, 50] and classification [13, 14] for 3D CT scans have been the subject of extensive research efforts in recent years. Recently, the Transformer-based visual feature extractor CT-ViT [47] has been introduced to deal with 3D CT scan efficiently, enabling the development of CT2Rep [10]. CT2Rep is the first method for automatic 3D CT scan radiology report generation, trained and evaluated on the CT-RATE public dataset [14]. CT2Rep is an auto-regressive model based on an encoder-decoder architecture [23], where visual features are extracted from the 3D CT scan using CT-ViT and then given to a Transformer Decoder [23, 41] that generates the report. However, end-to-end approaches [9, 10] do not guide the model to generate text conditionally based on upstream-detected abnormalities. In contrast, our approach builds upon previous work [22, 51] and introduces a step for abnormality classification to guide report generation based on previously predicted anomalies. This method thus offers greater control over the generation process.

3. DATASET

We use the CT-RATE public dataset [14] to train and evaluate our method. CT-RATE contains reconstructed non-contrast

3D chest CT volumes, corresponding reports and 18 distinct types of abnormalities extracted from reports using CXR-BERT [52]. Train set has 17,799 unique patient (34,781 volumes), validation set has 1,314 patients (3,075 volumes) and test set has 1,314 patients (3,039 volumes). We ensured there was no overlap of patients between the sets. Following [13, 14], all volumes are either center-cropped or padded to achieve a resolution of $240 \times 480 \times 480$ with a in-slice spacing of 0.75 mm and 1.5 mm in the z-axis. Hounsfield Unit (HU) [53] values are clipped between -1000 to $+200$ before normalization to $[-1, 1]$.

4. METHOD

4.1. Step 1: Multi-label classification pre-training

As illustrated in Figure 1, the model receives a volume $x \in \mathbb{R}^{240 \times 480 \times 480}$ as input. This volume is passed to a visual feature extractor Φ_V , either CT-Net [13] or CT-ViT [47]. CT-Net consists of ResNet [54] modules pre-trained on ImageNet [55] followed by a 3D convolutional network [56]. CT-ViT [47] is a Vision Transformer [40] based on the attention mechanism [41] computed from 3D patches extracted from the initial volume. From the initial volume x , both CT-Net and CT-ViT yield a vector representation $h \in \mathbb{R}^{512}$, such that:

$$h = \Phi_V(x). \quad (1)$$

Then, h is fed into a classification head Ψ to predict $\hat{y} \in \mathbb{R}^{18}$, as follows:

$$\hat{y} = \Psi(h), \quad (2)$$

where the components of the logit vector \hat{y} represent the anomaly scores for their respective class labels. Following a conventional approach for supervised multi-label classification [57], the model is trained using a binary cross-entropy loss function [58]. This initial step facilitates the training of a visual encoder Φ_V to extract salient visual features that enable accurate anomaly prediction.

4.2. Step 2: Multi-task single label classification

Starting from the previously pre-trained network, the multi-label classification head Ψ is replaced by 18 independent projection heads [59], denoted as Ψ_i^p ($i \in \{1, \dots, 18\}$), followed by classification heads denoted as Ψ_i^c ($i \in \{1, \dots, 18\}$). The feature vector h is first passed through each projection head Ψ_i^p to obtain a unique embedding noted h_i per class label, such that:

$$h_i = \Psi_i^p(h) \quad \forall i \in \{1, \dots, 18\}. \quad (3)$$

Subsequently, each embedding h_i is fed into its corresponding classification head Ψ_i^c . The classification head outputs an anomaly score $\hat{y}_i \in \mathbb{R}$ and employs a binary cross-entropy loss $\mathcal{L}_i \in \mathbb{R}$ as the objective function. The prediction step can be formalized as:

$$\hat{y}_i = \Psi_i^c(h_i) \quad \forall i \in \{1, \dots, 18\}. \quad (4)$$

Here, \hat{y}_i represents the predicted anomaly score for class i . The binary cross-entropy loss is then computed for each class, such that:

$$\mathcal{L}_i(\hat{y}_i, y_i) = -[y_i \log(\hat{y}_i) + (1 - y_i) \log(1 - \hat{y}_i)], \quad (5)$$

where $y_i \in \{0, 1\}$ denotes the ground-truth label for class i .

For each projection Ψ_i^p and classification Ψ_i^c head, back-propagation [60] of the corresponding parameters is performed solely based on the associated loss \mathcal{L}_i . For the rest of the neural network, back-propagation is carried out using the sum of these losses, denoted as $\mathcal{L} \in \mathbb{R}$. Introducing this supervised multi-task learning step enhances classification performance [61] and enables the extraction of a unique vector representation h_i for each abnormality i , conditioning sentence generation per abnormality in the subsequent step.

4.3. Step 3: Selection-based sentence generation

Abnormality selection In this report generation module, a description is generated for each abnormality predicted by the preceding classification module. During the training of this generation module, we consider only the labels correctly predicted as abnormal by the classification heads. During inference, we only consider labels predicted as abnormal by the corresponding classification heads. A label i is classified as abnormal if its predicted score \hat{y}_i exceeds a threshold

computed from the validation set, which maximizes the F1-Score [62, 63, 64].

Abnormality feature extraction For each label indexed by i and predicted as abnormal by its corresponding classification head Ψ_i^c , we extract and augment the corresponding embedding $h_i \in \mathbb{R}^{1024}$ to obtain a resulting vector $e_i \in \mathbb{R}^{18 \times 1024}$. This vector e_i contains zeros for all components associated with other abnormalities, while retaining the original embedding for the pathology corresponding i . We then employ a lightweight MLP Φ_T to project e_i from the visual latent space to the textual latent space, yielding $e_i^T \in \mathbb{R}^{1024}$, such that:

$$e_i^T = \Phi_T(e_i), \quad (6)$$

$$\text{where } e_i = [\vec{0}, \dots, \vec{0}, h_i, \vec{0}, \dots, \vec{0}]. \quad (7)$$

$\vec{0}$ denotes a zero vector of dimension 1024. This approach allows for a focused representation of the predicted abnormality within the multi-abnormality embedding space, while maintaining the context of the original embedding.

Sentence generation For each label i predicted as abnormal, we generate a descriptive sentence based on its associated embedding e_i^T . Inspired by prior work [22], the GPT-2 Medium Language model [65] fine-tuned on PubMed abstracts [66] is used for the Decoder part. GPT-2 is an auto-regressive model grounded in attention mechanism [41] where each embedded token only considers the contextual information provided by preceding tokens. Instead of using the conventional attention mechanism, the language model is conditioned on anomaly prediction by employing pseudo self-attention [67], noted PS . This approach injects the features associated with abnormality classification into the self-attention mechanism of GPT-2, such that:

$$PS(e_i^T, Y) = \text{softmax} \left((YW_q) \begin{bmatrix} e_i^T w_k \\ YW_k \end{bmatrix}^T \right) \begin{bmatrix} e_i^T w_v \\ YW_v \end{bmatrix}, \quad (8)$$

where w_k and w_v are the projection parameters for key and value vectors [41] for e_i^T ; W_k , W_q and W_v are the projection parameters for key, query and value for Y which are textual embedded tokens. During training, the model is trained on a next token prediction task [68] using a cross-entropy loss function [10, 22, 23]. All parameters are frozen except for those of GPT-2. During inference, only the CT scan and the [BOS] token [65] are fed into the model, which generates a description for each predicted abnormality.

Report generation The final report is generated by concatenating the generated sentences associated with each predicted anomaly.

5. EXPERIMENTAL SETUP

Training details. For the first and second steps, the model was trained with a batch size of 4, using the Adam [69] optimizer for 40 and 2 epochs, with a learning rate of 10^{-4} and

| Method | NLG Metrics | | | | | | CE Metrics | | |
|-------------------|--------------|--------------|--------------|----------------|--------------|---------------|--------------|--------------|--------------|
| | BL-1 | BL-4 | M | R _L | BERTs | BARTs | P | R | F1 |
| CT2Rep [10] | 0.323 | 0.115 | 0.176 | 0.241 | 0.864 | -3.178 | 0.416 | 0.367 | 0.360 |
| CT-AGRG w/ CT-ViT | 0.330 | 0.137 | 0.209 | 0.301 | 0.866 | -2.962 | 0.349 | 0.638 | 0.426 |
| CT-AGRG w/ CT-Net | 0.392 | 0.175 | 0.209 | 0.318 | 0.871 | -2.900 | 0.443 | 0.650 | 0.515 |

| <i>Ablation study</i> | | | | | | | | | |
|----------------------------|---------------------------|------------------------|----------------|--------------|--------------|--------------|--------------|--------------|--|
| Multi-label classification | Multi-task classification | Augmented Latent Space | Language model | BL-4 | M | P | R | F1 | |
| ✓ | | | ✓ | 0.083 | 0.127 | 0.404 | 0.190 | 0.208 | |
| ✓ | ✓ | | ✓ | 0.171 | 0.194 | 0.429 | 0.617 | 0.492 | |
| ✓ | | ✓ | ✓ | 0.151 | 0.197 | 0.430 | 0.640 | 0.503 | |
| ✓ | ✓ | ✓ | ✓ | 0.175 | 0.209 | 0.443 | 0.650 | 0.515 | |

Table 1: Quantitative evaluation on the test set with Natural Language Generation (NLG) metrics and Clinical Efficacy (CE) metrics. Our model outperforms the previous method both on NLG and CE metrics. *Ablation study*: The evaluation on NLG and CE metrics highlights the contribution of each module of our method. The ablation study on CT-AGRG was conducted with CT-Net [13] as visual feature extractor, since it yields the best results.

10^{-5} , respectively. For the third step, training was conducted for 50 epochs with a batch size of 64, using the AdamW [70] optimizer with a learning rate of 5×10^{-5} . The training required a GPU with 48GB of memory.

Generation mode. Generated sentences were limited to 60 tokens [71], typically the maximum observed per sentence in the report corpus. At inference, we use the Beam Search [72, 73, 74] algorithm as generation mode [75, 76, 77, 78]. Beam size is set to 4, aligning with prior work and balancing output quality with computational efficiency. [10, 22, 23].

6. RESULTS

6.1. Quantitative results

As commonly practiced, abnormalities mentioned in the generated report are extracted with the CXR-BERT labeler [52]. Analogous to a classification problem, these predicted anomalies are compared against ground truth labels to compute Clinical Efficacy (CE) metrics: Precision, Recall, and F1-Score [79]. We also evaluate our captioning model using widely used [10, 22, 23, 26] Natural Language Generation (NLG) metrics: BLEU-1 and BLEU-4 [80] for n-gram precision; METEOR [81] for alignment with stemming and synonymy; ROUGE [82] for overlap focusing on recall; BERT-Score [83] for token-level contextual embedding similarity; and BART-Score [84] for sequence-level likelihood assessment. This combination captures lexical, semantic, and generative aspects of caption quality, providing a comprehensive evaluation of our model’s performance [85, 86]. Table 1 demonstrates that CT-AGRG achieves significantly better results than prior work. With CT-ViT and CT-Net as visual feature extractors, we achieve an average Recall of

0.638 and 0.650 ($\Delta+74\%$ and $\Delta+77\%$ increase compared to CT2Rep [10]), and an average F1-Score of 0.426 and 0.515, respectively ($\Delta+18\%$ and $\Delta+43\%$ increase). CT-AGRG achieves a BARTScore [84] of -2.900, outperforming CT2Rep [10] (-3.178, $\Delta+9\%$ increase), indicating enhanced abnormality detection capabilities and improved semantic relevance in generated captions.

6.2. Ablation study

As shown in Table 1, we conduct an ablation study to evaluate each component of our CT-AGRG model. Introducing multi-task classification significantly improves F1-Score from 0.208 to 0.492 ($\Delta+136\%$ increase). Augmenting the latent space further enhances performance, increasing Recall from 0.617 to 0.650 ($\Delta+5\%$ increase) and F1-Score from 0.492 to 0.515 ($\Delta+5\%$ increase). NLG metrics show notable improvements, with BLEU-4 [80] and METEOR [81] scores increasing by 0.092 and 0.082, respectively, indicating enhanced sentence variability while maintaining semantic fidelity to ground truth reports.

7. CONCLUSION

In this paper, we have presented a simple yet effective method for guided report generation. Our approach, based on conditional description generation for each abnormality, outperforms state-of-the-art methods while offering a high level of control over the generated report. Future work could focus on adapting the approach to require less supervision, leveraging other modalities or region-specific data to further enhance the report generation process.

8. REFERENCES

- [1] Satya P. Singh, Lipo Wang, Sukrit Gupta, Haveesh Goli, Parasuraman Padmanabhan, and Balázs Gulyás, “3D Deep Learning on Medical Images: A Review,” *Sensors (Basel, Switzerland)*, vol. 20, no. 18, pp. 5097, Sept. 2020.
- [2] Erik P. Hess, Lindsey R. Haas, Nilay D. Shah, Robert J. Stroebel, Charles R. Denham, and Stephen J. Swensen, “Trends in computed tomography utilization rates: a longitudinal practice-based study,” *Journal of Patient Safety*, vol. 10, no. 1, pp. 52–58, Mar. 2014.
- [3] Joshua Broder and David M. Warshauer, “Increasing utilization of computed tomography in the adult emergency department, 2000-2005,” *Emergency Radiology*, vol. 13, no. 1, pp. 25–30, Oct. 2006.
- [4] M. Fernanda Bellolio, Herbert C. Heien, Lindsey R. Sangaralingham, Molly M. Jeffery, Ronna L. Campbell, Daniel Cabrera, Nilay D. Shah, and Erik P. Hess, “Increased Computed Tomography Utilization in the Emergency Department and Its Association with Hospital Admission,” *The Western Journal of Emergency Medicine*, vol. 18, no. 5, pp. 835–845, Aug. 2017.
- [5] Stacy K. Goergen, Felicity J. Pool, Tari J. Turner, Jane E. Grimm, Mark N. Appleyard, Carmel Crock, Michael C. Fahey, Michael F. Fay, Nicholas J. Ferris, Susan M. Liew, Richard D. Perry, Ann Revell, Grant M. Russell, Shih-Chang S. C. Wang, and Christian Wriedt, “Evidence-based guideline for the written radiology report: methods, recommendations and implementation challenges,” *Journal of Medical Imaging and Radiation Oncology*, vol. 57, no. 1, pp. 1–7, Feb. 2013.
- [6] Sarah Bastawrous and Benjamin Carney, “Improving Patient Safety: Avoiding Unread Imaging Exams in the National VA Enterprise Electronic Health Record,” *Journal of Digital Imaging*, vol. 30, no. 3, pp. 309–313, June 2017.
- [7] Abi Rimmer, “Radiologist shortage leaves patient care at risk, warns royal college,” *BMJ (Clinical research ed.)*, vol. 359, pp. j4683, Oct. 2017.
- [8] Erik Ranschaert, Laurens Topff, and Oleg Pianykh, “Optimization of Radiology Workflow with Artificial Intelligence,” *Radiologic Clinics of North America*, vol. 59, no. 6, pp. 955–966, Nov. 2021.
- [9] Che Liu, Zhongwei Wan, Yuqi Wang, Hui Shen, Haozhe Wang, Kangyu Zheng, Mi Zhang, and Rossella Arcucci, “Benchmarking and Boosting Radiology Report Generation for 3D High-Resolution Medical Images,” June 2024, arXiv:2406.07146 [cs].
- [10] Ibrahim Ethem Hamamci, Sezgin Er, and Bjoern Menze, “CT2Rep: Automated Radiology Report Generation for 3D Medical Imaging,” Mar. 2024, arXiv:2403.06801 [cs, eess].
- [11] Alistair E. W. Johnson, Tom Pollard, Roger Mark, Seth Berkowitz, and Steven Horng, “The MIMIC-CXR Database,” 2019.
- [12] Jeremy Irvin, Pranav Rajpurkar, Michael Ko, Yifan Yu, Silviana Ciurea-Ilcus, Chris Chute, Henrik Marklund, Behzad Haghgo, Robyn Ball, Katie Shpanskaya, Jayne Seekins, David A. Mong, Safwan S. Halabi, Jesse K. Sandberg, Ricky Jones, David B. Larson, Curtis P. Langlotz, Bhavik N. Patel, Matthew P. Lungren, and Andrew Y. Ng, “CheXpert: A Large Chest Radiograph Dataset with Uncertainty Labels and Expert Comparison,” Jan. 2019, arXiv:1901.07031 [cs, eess].
- [13] Rachel Lea Draelos, David Dov, Maciej A. Mazurowski, Joseph Y. Lo, Ricardo Henao, Geoffrey D. Rubin, and Lawrence Carin, “Machine-learning-based multiple abnormality prediction with large-scale chest computed tomography volumes,” *Medical Image Analysis*, vol. 67, pp. 101857, Jan. 2021.
- [14] Ibrahim Ethem Hamamci, Sezgin Er, Furkan Almas, Ayse Gulnihan Simsek, Seval Nil Esirgun, Irem Dogan, Muhammed Furkan Dasdelen, Bastian Wittmann, Enis Simsar, Mehmet Simsar, Emine Bensu Erdemir, Abdullah Alanbay, Anjany Sekuboyina, Berkcan Lafci, Mehmet K. Ozdemir, and Bjoern Menze, “A foundation model utilizing chest CT volumes and radiology reports for supervised-level zero-shot detection of abnormalities,” Mar. 2024, arXiv:2403.17834 [cs].
- [15] “Deep-chest: Multi-classification deep learning model for diagnosing COVID-19, pneumonia, and lung cancer chest diseases - ScienceDirect,”
- [16] Arshia Rehman, Ahmad Khan, Gohar Fatima, Saeeda Naz, and Imran Razzak, “Review on chest pathologies detection systems using deep learning techniques,” *Artificial Intelligence Review*, vol. 56, no. 11, pp. 12607–12653, Nov. 2023.
- [17] Abhishek K. Dubey, Michael T. Young, Christopher Stanley, Dalton Lunga, and Jacob Hinkle, “Computer-aided abnormality detection in chest radiographs in a clinical setting via domain-adaptation,” Dec. 2020, arXiv:2012.10564 [cs].
- [18] Kyungsu Kim, Seong Je Oh, Ju Hwan Lee, and Myung Jin Chung, “3D unsupervised anomaly detection through virtual multi-view projection and reconstruction: Clinical validation on low-dose chest computed tomography,” *Expert Systems with Applications*, vol. 236, pp. 121165, Feb. 2024.

[19] Neeraj Dhungel, Gustavo Carneiro, and Andrew P. Bradley, “Deep Learning and Structured Prediction for the Segmentation of Mass in Mammograms,” in *Medical Image Computing and Computer-Assisted Intervention – MICCAI 2015*, Nassir Navab, Joachim Hornegger, William M. Wells, and Alejandro Frangi, Eds., vol. 9349, pp. 605–612. Springer International Publishing, Cham, 2015, Series Title: Lecture Notes in Computer Science.

[20] Dinh Van Chi Mai, Ioanna Drami, Edward T. Pring, Laura E. Gould, Phillip Lung, Karteek Popuri, Vincent Chow, Mirza F. Beg, Thanos Athanasiou, and John T. Jenkins, “A systematic review of automated segmentation of 3D computed-tomography scans for volumetric body composition analysis,” *Journal of Cachexia, Sarcopenia and Muscle*, vol. 14, no. 5, pp. 1973–1986, Aug. 2023.

[21] Ademola E. Ilesanmi, Taiwo O. Ilesanmi, and Babatunde O. Ajayi, “Reviewing 3D convolutional neural network approaches for medical image segmentation,” *Heliyon*, vol. 10, no. 6, pp. e27398, Mar. 2024.

[22] Tim Tanida, Philip Müller, Georgios Kaassis, and Daniel Rueckert, “Interactive and Explainable Region-guided Radiology Report Generation,” in *2023 IEEE/CVF Conference on Computer Vision and Pattern Recognition (CVPR)*, June 2023, pp. 7433–7442, arXiv:2304.08295 [cs].

[23] Zhihong Chen, Yan Song, Tsung-Hui Chang, and Xiang Wan, “Generating Radiology Reports via Memory-driven Transformer,” Apr. 2022, arXiv:2010.16056 [cs].

[24] Baoyu Jing, Zeya Wang, and Eric Xing, “Show, Describe and Conclude: On Exploiting the Structure Information of Chest X-Ray Reports,” in *Proceedings of the 57th Annual Meeting of the Association for Computational Linguistics*, 2019, pp. 6570–6580, arXiv:2004.12274 [cs, eess].

[25] Baoyu Jing, Pengtao Xie, and Eric Xing, “On the Automatic Generation of Medical Imaging Reports,” in *Proceedings of the 56th Annual Meeting of the Association for Computational Linguistics (Volume 1: Long Papers)*, Iryna Gurevych and Yusuke Miyao, Eds., Melbourne, Australia, July 2018, pp. 2577–2586, Association for Computational Linguistics.

[26] Isabel Rio-Torto, Jaime S Cardoso, and Luis F Teixeira, “Parameter-Efficient Generation of Natural Language Explanations for Chest X-ray Classification,” .

[27] Raphael Stock, Stefan Denner, Yannick Kirchhoff, Constantin Ulrich, Maximilian Rouven Rokuss, Saikat Roy, Nico Disch, and Klaus Maier-Hein, “From Generalist to Specialist: Incorporating Domain-Knowledge into Flamingo for Chest X-Ray Report Generation,” Apr. 2024.

[28] Lloyd J. Ridley, “Guide to the radiology report,” *Australasian Radiology*, vol. 46, no. 4, pp. 366–369, Dec. 2002.

[29] Danna Gurari, Qing Li, Abigale J. Stangl, Anhong Guo, Chi Lin, Kristen Grauman, Jiebo Luo, and Jeffrey P. Bigham, “VizWiz Grand Challenge: Answering Visual Questions from Blind People,” May 2018, arXiv:1802.08218 [cs].

[30] Haochen Xue, Chong Zhang, Chengzhi Liu, Fangyu Wu, and Xiaobo Jin, “Multi-task Prompt Words Learning for Social Media Content Generation,” July 2024, arXiv:2407.07771 [cs] version: 1.

[31] Oriol Vinyals, Alexander Toshev, Samy Bengio, and Dumitru Erhan, “Show and Tell: A Neural Image Caption Generator,” Apr. 2015, arXiv:1411.4555 [cs].

[32] Xiangrong Zhang, Xin Wang, Xu Tang, Huiyu Zhou, and Chen Li, “Remote Sensing | Free Full-Text | Description Generation for Remote Sensing Images Using Attribute Attention Mechanism,” .

[33] Dave Zhenyu Chen, Ronghang Hu, Xinlei Chen, Matthias Nießner, and Angel X. Chang, “UniT3D: A Unified Transformer for 3D Dense Captioning and Visual Grounding,” Dec. 2022, arXiv:2212.00836 [cs].

[34] Haoran Wang, Yue Zhang, and Xiaosheng Yu, “An Overview of Image Caption Generation Methods,” *Computational Intelligence and Neuroscience*, vol. 2020, pp. 3062706, Jan. 2020.

[35] Marco López-Sánchez, Betania Hernández-Ocaña, Oscar Chávez-Bosquez, and José Hernández-Torruco, “Supervised Deep Learning Techniques for Image Description: A Systematic Review,” *Entropy*, vol. 25, no. 4, pp. 553, Mar. 2023.

[36] Gaurav and Pratistha Mathur, “A Survey on Various Deep Learning Models for Automatic Image Captioning,” *Journal of Physics: Conference Series*, vol. 1950, no. 1, pp. 012045, Aug. 2021, Publisher: IOP Publishing.

[37] Ting Pang, Peigao Li, and Lijie Zhao, “A survey on automatic generation of medical imaging reports based on deep learning,” *BioMedical Engineering OnLine*, vol. 22, pp. 48, May 2023.

[38] “y?brid retrieval-generation reinforced agent for medical image report generation - Recherche Google,” .

[39] Keiron O’Shea and Ryan Nash, “An Introduction to Convolutional Neural Networks,” Dec. 2015, arXiv:1511.08458 [cs].

[40] Alexey Dosovitskiy, Lucas Beyer, Alexander Kolesnikov, Dirk Weissenborn, Xiaohua Zhai, Thomas Unterthiner, Mostafa Dehghani, Matthias Minderer, Georg Heigold, Sylvain Gelly, Jakob Uszkoreit, and Neil Houlsby, “An Image is Worth 16x16 Words: Transformers for Image Recognition at Scale,” June 2021, arXiv:2010.11929 [cs].

[41] Ashish Vaswani, Noam Shazeer, Niki Parmar, Jakob Uszkoreit, Llion Jones, Aidan N. Gomez, Łukasz Kaiser, and Illia Polosukhin, “Attention Is All You Need,” Aug. 2023, arXiv:1706.03762 [cs].

[42] Alex Sherstinsky, “Fundamentals of Recurrent Neural Network (RNN) and Long Short-Term Memory (LSTM) Network,” *Physica D: Nonlinear Phenomena*, vol. 404, pp. 132306, Mar. 2020, arXiv:1808.03314 [cs, stat].

[43] Di You, Fenglin Liu, Shen Ge, Xiaoxia Xie, Jing Zhang, and Xian Wu, “AlignTransformer: Hierarchical Alignment of Visual Regions and Disease Tags for Medical Report Generation,” Mar. 2022, arXiv:2203.10095 [cs, eess].

[44] “Large Model driven Radiology Report Generation with Clinical Quality Reinforcement Learning.”

[45] Farhad Nooralahzadeh, Nicolas Perez Gonzalez, Thomas Frauenfelder, Koji Fujimoto, and Michael Krauthammer, “Progressive Transformer-Based Generation of Radiology Reports,” Aug. 2021, arXiv:2102.09777 [cs].

[46] Guanxiong Liu, Tzu-Ming Harry Hsu, Matthew McDermott, Willie Boag, Wei-Hung Weng, Peter Szolovits, and Marzyeh Ghassemi, “Clinically Accurate Chest X-Ray Report Generation,” July 2019, arXiv:1904.02633 [cs].

[47] Ibrahim Ethem Hamamci, Sezgin Er, Anjany Sekuboina, Enis Simsar, Alperen Tezcan, Ayse Gulnihan Simsek, Seval Nil Esirgun, Furkan Almas, Irem Dogan, Muhammed Furkan Dasdelen, Chinmay Prabhakar, Hadrien Reynaud, Sarthak Pati, Christian Bluethgen, Mehmet Kemal Ozdemir, and Bjoern Menze, “GenerateCT: Text-Conditional Generation of 3D Chest CT Volumes,” Mar. 2024, arXiv:2305.16037 [cs].

[48] Fan Bai, Yuxin Du, Tiejun Huang, Max Q.-H. Meng, and Bo Zhao, “M3D: Advancing 3D Medical Image Analysis with Multi-Modal Large Language Models,” Mar. 2024, arXiv:2404.00578 [cs].

[49] Chaoyi Wu, Xiaoman Zhang, Ya Zhang, Yanfeng Wang, and Weidi Xie, “Towards Generalist Foundation Model for Radiology by Leveraging Web-scale 2D&3D Medical Data,” Nov. 2023, arXiv:2308.02463 [cs].

[50] Aissam Djahnine, Carole Lazarus, Mathieu Lederlin, Sébastien Mulé, Rafael Wiemker, Salim Si-Mohamed, Emilien Jupin-Delevaux, Olivier Nempong, Youssef Skandarani, Mathieu De Craene, Segbedji Goubalan, Caroline Raynaud, Younes Belkouchi, Amira Ben Afia, Clement Fabre, Gilbert Ferretti, Constance De Margerie, Pierre Berge, Renan Liberge, Nicolas Elbaz, Maxime Blain, Pierre-Yves Brillet, Guillaume Chassagnon, Farah Cadour, Caroline Caramella, Mostafa El Hajjam, Samia Boussouar, Joya Hadchiti, Xavier Fablet, Antoine Khalil, Hugues Talbot, Alain Luciani, Nathalie Lassau, and Loic Boussel, “Detection and severity quantification of pulmonary embolism with 3D CT data using an automated deep learning-based artificial solution,” *Diagnostic and Interventional Imaging*, vol. 105, no. 3, pp. 97–103, Mar. 2024.

[51] Lin Wang, Munan Ning, Donghuan Lu, Dong Wei, Yefeng Zheng, and Jie Chen, “An Inclusive Task-Aware Framework for Radiology Report Generation,” in *Medical Image Computing and Computer Assisted Intervention – MICCAI 2022*, Linwei Wang, Qi Dou, P. Thomas Fletcher, Stefanie Speidel, and Shuo Li, Eds., Cham, 2022, pp. 568–577, Springer Nature Switzerland.

[52] Benedikt Boecking, Naoto Usuyama, Shruthi Bannur, Daniel C. Castro, Anton Schwaighofer, Stephanie Hyland, Maria Wetscherek, Tristan Naumann, Aditya Nori, Javier Alvarez-Valle, Hoifung Poon, and Ozan Oktay, “Making the Most of Text Semantics to Improve Biomedical Vision–Language Processing,” in *Computer Vision – ECCV 2022*, Shai Avidan, Gabriel Brostow, Moustapha Cissé, Giovanni Maria Farinella, and Tal Hassner, Eds., Cham, 2022, pp. 1–21, Springer Nature Switzerland.

[53] Tami D. DenOtter and Johanna Schubert, “Hounsfield Unit,” in *StatPearls*. StatPearls Publishing, Treasure Island (FL), 2024.

[54] Kaiming He, Xiangyu Zhang, Shaoqing Ren, and Jian Sun, “Deep Residual Learning for Image Recognition,” Dec. 2015, arXiv:1512.03385 [cs].

[55] “ImageNet: A large-scale hierarchical image database | IEEE Conference Publication | IEEE Xplore.”

[56] Du Tran, Lubomir Bourdev, Rob Fergus, Lorenzo Torresani, and Manohar Paluri, “Learning Spatiotemporal Features with 3D Convolutional Networks,” Oct. 2015, arXiv:1412.0767 [cs].

[57] Jasmin Bogatinovski, Ljupčo Todorovski, Sašo Džeroski, and Dragi Kocev, “Comprehensive comparative study of multi-label classification methods,” *Expert Systems with Applications*, vol. 203, pp. 117215, Oct. 2022.

[58] I. J. Good, “Rational Decisions,” *Journal of the Royal Statistical Society. Series B (Methodological)*, vol. 14, no. 1, pp. 107–114, 1952, Publisher: [Royal Statistical Society, Wiley].

[59] Ting Chen, Simon Kornblith, Mohammad Norouzi, and Geoffrey Hinton, “A Simple Framework for Contrastive Learning of Visual Representations,” June 2020, arXiv:2002.05709 [cs, stat].

[60] Yann Lecun, “A Theoretical Framework for Back-Propagation,” Aug. 2001.

[61] Michael Crawshaw, “Multi-Task Learning with Deep Neural Networks: A Survey,” Sept. 2020, arXiv:2009.09796 [cs, stat].

[62] David M. W. Powers, “Evaluation: from precision, recall and F-measure to ROC, informedness, markedness and correlation,” Oct. 2020, arXiv:2010.16061 [cs, stat].

[63] Yutaka Sasaki, “The truth of the F-measure.” .

[64] Geert Litjens, Thijs Kooi, Babak Ehteshami Bejnordi, Arnaud Arindra Adiyoso Setio, Francesco Ciompi, Mohsen Ghafoorian, Jeroen A. W. M. van der Laak, Bram van Ginneken, and Clara I. Sánchez, “A survey on deep learning in medical image analysis,” *Medical Image Analysis*, vol. 42, pp. 60–88, 2017.

[65] Alec Radford, Jeffrey Wu, Rewon Child, David Luan, Dario Amodei, and Ilya Sutskever, “Language Models are Unsupervised Multitask Learners,” .

[66] Yannis Papanikolaou and Andrea Pierleoni, “DARE: Data Augmented Relation Extraction with GPT-2,” Apr. 2020, arXiv:2004.13845 [cs, stat].

[67] Zachary M. Ziegler, Luke Melas-Kyriazi, Sebastian Gehrmann, and Alexander M. Rush, “Encoder-Agnostic Adaptation for Conditional Language Generation,” Sept. 2019, arXiv:1908.06938 [cs].

[68] Yoshua Bengio, Réjean Ducharme, Pascal Vincent, and Christian Jauvin, “A Neural Probabilistic Language Model,” .

[69] Diederik P. Kingma and Jimmy Ba, “Adam: A Method for Stochastic Optimization,” Jan. 2017, arXiv:1412.6980 [cs].

[70] Ilya Loshchilov and Frank Hutter, “Decoupled Weight Decay Regularization,” Jan. 2019, arXiv:1711.05101 [cs, math].

[71] Mosh Levy, Alon Jacoby, and Yoav Goldberg, “Same Task, More Tokens: the Impact of Input Length on the Reasoning Performance of Large Language Models,” Feb. 2024, arXiv:2402.14848 [cs].

[72] Bruce T Lowerre, “THE HARPY SPEECH RECOGNITION SYSTEM,” .

[73] Markus Freitag and Yaser Al-Onaizan, “Beam Search Strategies for Neural Machine Translation,” in *Proceedings of the First Workshop on Neural Machine Translation*, 2017, pp. 56–60, arXiv:1702.01806 [cs].

[74] Clara Meister, Tim Vieira, and Ryan Cotterell, “Best-First Beam Search,” Nov. 2022, arXiv:2007.03909 [cs].

[75] Daniel Jurafsky and James H Martin, *Speech and Language Processing: An Introduction to Natural Language Processing, Computational Linguistics, and Speech Recognition*, Prentice Hall, Upper Saddle River, NJ, 2 edition, 2009.

[76] Junyi Li, Tianyi Tang, Wayne Xin Zhao, Jian-Yun Nie, and Ji-Rong Wen, “Pretrained Language Models for Text Generation: A Survey,” May 2022, arXiv:2201.05273 [cs].

[77] Ashwin K. Vijayakumar, Michael Cogswell, Ram-prasath R. Selvaraju, Qing Sun, Stefan Lee, David Crandall, and Dhruv Batra, “Diverse Beam Search: Decoding Diverse Solutions from Neural Sequence Models,” Oct. 2018, arXiv:1610.02424 [cs].

[78] “Hierarchical Neural Story Generation - ACL Anthology,” .

[79] C. J. van Rijsbergen, *Information Retrieval*, Butterworth-Heinemann, 1979.

[80] Kishore Papineni, Salim Roukos, Todd Ward, and Wei-Jing Zhu, “Bleu: a Method for Automatic Evaluation of Machine Translation,” in *Proceedings of the 40th Annual Meeting of the Association for Computational Linguistics*, Pierre Isabelle, Eugene Charniak, and Dekang Lin, Eds., Philadelphia, Pennsylvania, USA, July 2002, pp. 311–318, Association for Computational Linguistics.

[81] Alon Lavie and Michael J. Denkowski, “The Meteor metric for automatic evaluation of machine translation,” *Machine Translation*, vol. 23, no. 2, pp. 105–115, Sept. 2009.

[82] *Text Summarization Branches Out*, Association for Computational Linguistics, Barcelona, Spain, July 2004.

- [83] Tianyi Zhang, Varsha Kishore, Felix Wu, Kilian Q. Weinberger, and Yoav Artzi, “BERTScore: Evaluating Text Generation with BERT,” Feb. 2020, arXiv:1904.09675 [cs].
- [84] Weizhe Yuan, Graham Neubig, and Pengfei Liu, “BARTScore: Evaluating Generated Text as Text Generation,” Oct. 2021, arXiv:2106.11520 [cs].
- [85] Maxime Kayser, Oana-Maria Camburu, Leonard Salewski, Cornelius Emde, Virginie Do, Zeynep Akata, and Thomas Lukasiewicz, “e-ViL: A Dataset and Benchmark for Natural Language Explanations in Vision-Language Tasks,” Aug. 2021, arXiv:2105.03761 [cs].
- [86] Maxime Kayser, Cornelius Emde, Oana-Maria Camburu, Guy Parsons, Bartłomiej Papiez, and Thomas Lukasiewicz, “Explaining Chest X-ray Pathologies in Natural Language,” July 2022, arXiv:2207.04343 [cs].

A. QUANTITATIVE RESULTS

| Abnormality | CT2Rep | | | CT-AGRG (Ours) | | | Frequency |
|------------------------------------|--------|-------|-------|----------------|--------------|--------------|-----------|
| | P | R | F1 | P | R | F1 | |
| Medical material | 0.461 | 0.120 | 0.190 | <u>0.630</u> | <u>0.443</u> | <u>0.521</u> | 0.114 |
| Arterial wall calcification | 0.679 | 0.751 | 0.713 | <u>0.681</u> | <u>0.872</u> | <u>0.765</u> | 0.267 |
| Cardiomegaly | 0.476 | 0.422 | 0.447 | <u>0.488</u> | <u>0.774</u> | <u>0.599</u> | 0.108 |
| Pericardial effusion | 0.136 | 0.085 | 0.105 | <u>0.269</u> | <u>0.505</u> | <u>0.351</u> | 0.074 |
| Coronary artery wall calcification | 0.690 | 0.701 | 0.696 | 0.660 | <u>0.880</u> | <u>0.755</u> | 0.244 |
| Hiatal hernia | 0.186 | 0.510 | 0.273 | <u>0.217</u> | <u>0.701</u> | <u>0.331</u> | 0.134 |
| Lymphadenopathy | 0.345 | 0.526 | 0.417 | <u>0.397</u> | <u>0.646</u> | <u>0.491</u> | 0.266 |
| Emphysema | 0.311 | 0.479 | 0.377 | <u>0.423</u> | <u>0.431</u> | <u>0.427</u> | 0.195 |
| Atelectasis | 0.348 | 0.267 | 0.302 | <u>0.356</u> | <u>0.610</u> | <u>0.450</u> | 0.232 |
| Lung nodule | 0.547 | 0.732 | 0.626 | <u>0.622</u> | <u>0.853</u> | <u>0.719</u> | 0.425 |
| Lung opacity | 0.841 | 0.431 | 0.570 | 0.680 | <u>0.787</u> | <u>0.729</u> | 0.374 |
| Pulmonary fibrotic sequela | 0.358 | 0.317 | 0.337 | <u>0.393</u> | <u>0.724</u> | <u>0.509</u> | 0.267 |
| Pleural effusion | 0.716 | 0.439 | 0.544 | 0.639 | <u>0.800</u> | <u>0.710</u> | 0.126 |
| Mosaic attenuation pattern | 0.172 | 0.315 | 0.223 | <u>0.271</u> | <u>0.533</u> | <u>0.359</u> | 0.078 |
| Peribronchial thickening | 0.213 | 0.122 | 0.155 | <u>0.233</u> | <u>0.589</u> | <u>0.334</u> | 0.098 |
| Consolidation | 0.456 | 0.303 | 0.364 | <u>0.459</u> | <u>0.653</u> | <u>0.539</u> | 0.172 |
| Bronchiectasis | 0.357 | 0.032 | 0.058 | 0.294 | <u>0.468</u> | <u>0.362</u> | 0.099 |
| Interlobular septal thickening | 0.200 | 0.053 | 0.084 | <u>0.260</u> | <u>0.426</u> | <u>0.323</u> | 0.071 |
| Mean | 0.416 | 0.367 | 0.360 | <u>0.443</u> | <u>0.650</u> | <u>0.515</u> | 0.186 |

Table 2: Quantitative evaluation on the test set with Precision (P), Recall (R) and F1-Score (F1) for each pathology. Frequency of each pathology in the test set is also provided. The metrics associated with CT-AGRG were computed using CT-Net [13] as the visual feature extractor, as this configuration yielded the best performance. The underlined metrics are those that have improved with our contribution compared to the previous method. Our method improves the classification metrics for the majority of abnormalities.

B. QUALITATIVE RESULTS



Ground truth

A millimetric calcific atherosclerotic plaque was observed in the wall of the thoracic aorta. Sliding type hiatal hernia was observed. A few millimetric nonspecific parenchymal nodules were observed in both lungs. When examined in the lung parenchyma window; mosaic attenuation pattern was observed in both lungs.

Generation with CT2Rep

There are atherosomatous plaques in the aorta. There is a sliding type hiatal hernia at the lower end of the esophagus. There are millimetric nonspecific nodules in both lungs.

Generation with CT-GRG

Atheroma plaques are observed in the aorta and coronary arteries. Sliding type hiatal hernia was observed at the lower end of the esophagus. There are millimetric nonspecific nodules in both lungs. When examined in the lung parenchyma window; mosaic attenuation pattern is observed in both lungs.



Ground truth

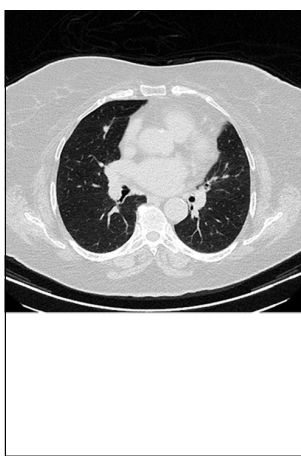
Diffuse atheroma plaques are observed in the aorta and coronary arteries. There are atelectasis in both lower lobes of the lungs adjacent to the pleural effusion. Bilateral pleural effusion is observed. There are minimal emphysematous changes in both lungs.

Generation with CT2Rep

There are calcified atherosomatous plaques on the walls of the thoracic aorta and coronary vascular structures. There is a sliding type hiatal hernia at the lower end.

Generation with CT-GRG

Calcific atheroma plaques are observed in the aorta and coronary arteries. When examined in the lung parenchyma window atelectatic changes were observed in the lower lobes of both lungs. There is bilateral minimal pleural effusion. Heart size increased. There is minimal pericardial effusion.



Ground truth

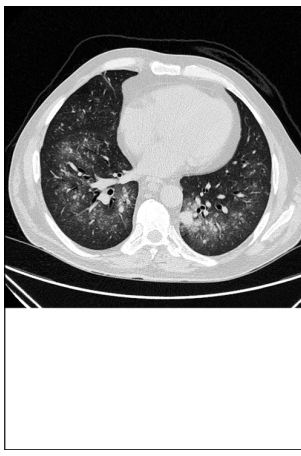
Millimetric calcific atheroma plaques are observed in the anterior descending coronary artery and aorta. Sliding type hiatal hernia is observed at the esophagogastric junction. Atelectasis and local volume loss are observed in the left lung upper lobe lingular segment inferior subsegment, right lung middle lobe medial segment, left lung lower lobe medial segment. Minimal emphysematous changes are present in both lungs. Approximately 10 nodules are observed in both lungs, the largest of which is in the medial segment of the middle lobe, with a perifissure location of 6x7.

Generation with CT2Rep

Calcified atherosclerotic changes were observed in the wall of the thoracic aorta and coronary artery. Sliding type hiatal hernia was observed. Heart size increased. When examined in the lung parenchyma window mosaic attenuation pattern was observed in both lungs small airway disease small vessel disease

Generation with CT-GRG

Calcified atherosclerotic changes were observed in the wall of the thoracic aorta and coronary artery. Sliding type hiatal hernia was observed at the lower end of the esophagus. When examined in the lung parenchyma window linear atelectasis was observed in the lower lobes of both lungs. There are emphysematous changes in both lungs. There are millimetric nonspecific nodules in both lungs. There are millimetric lymph nodes in the mediastinum. When examined in the lung parenchyma window pleuroparenchymal sequelae density increases were observed in both lungs.



Ground truth

Subsegmental atelectatic changes were observed in the medial segment of the right lung middle lobe. Centriacinar nodular infiltrates tend to coalesce with each other and occasionally to form focal consolidation. When examined in the lung parenchyma window; There are diffuse ground glass areas in both lungs, miliary and centriacinar nodular infiltrates at this level. There are bilateral axillary upper, lower paratracheal, anterior prevascular, aortopulmonary, subcarinal, bilateral hilar, paraesophageal multiple lymph nodes, the largest of which is 22.

Generation with CT2Rep

In the evaluation of both lung parenchyma diffuse ground glass densities and consolidations are observed in both lung parenchyma. Right upper bilateral lower paratracheal millimetric lymph node is observed. In the evaluation of both lung parenchyma mosaic attenuation is observed in both lung parenchyma. The cardiothoracic index increased in favor of the heart.

Generation with CT-GRG

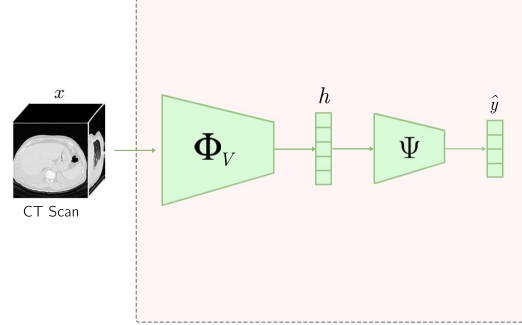
When examined in the lung parenchyma window subsegmental atelectatic changes were observed in the lower lobes of both lungs. When examined in the lung parenchyma window in both lungs there are areas of consolidation in which air bronchograms are observed. When examined in the lung parenchyma window widespread patchy ground glass densities are observed in both lungs. There are lymph nodes in the mediastinum and hilar regions. There is minimal pericardial effusion. When examined in the lung parenchyma window peribronchial thickenings were observed in both lungs.

Fig. 2: Comparison of ground truth with generated reports with CT2Rep [10] and CT-AGR on test set from CT-RATE [14].

C. TRAINING STEPS

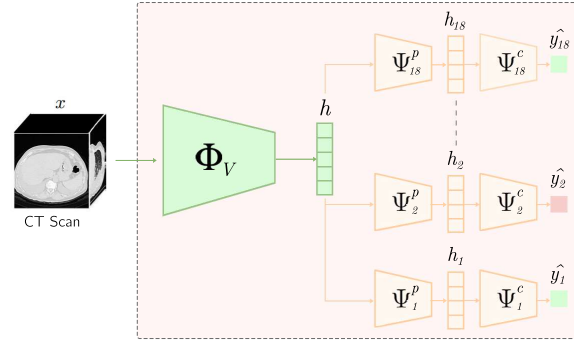
Step 1: Multi-label classification pre-training

Φ_V, Ψ are trained from scratch.



Step 2: Multi-task single label classification

Φ_V is fine-tuned from weights extracted from Step 1.
 Ψ_i^p, Ψ_i^c are trained from scratch.



Step 3: Report generation

$\Phi_V, \Psi_i^p, \Psi_i^c$ parameters are frozen.
 Φ_T is trained from scratch.
GPT-2 is fine-tuned from pre-trained weights on PubMed abstracts.

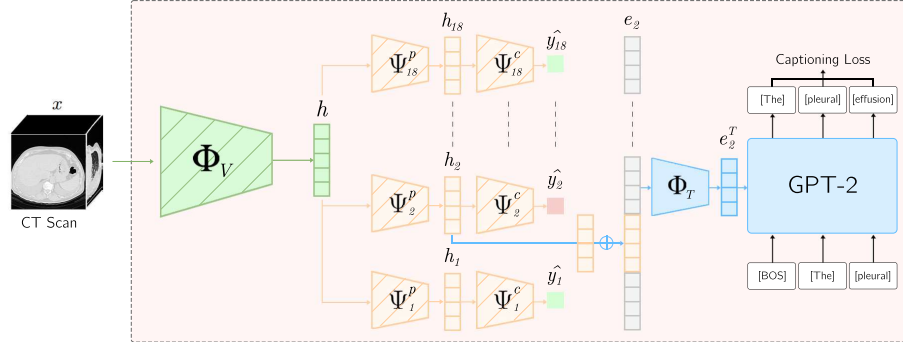


Fig. 3: Overview of the method with details for each step.

D. HYPERPARAMETERS

| | Step 1 | Step 1 | Step 2 | Step 2 |
|---|----------------|----------------|----------------|----------------|
| | w/ CT-Net [13] | w/ CT-ViT [47] | w/ CT-Net [13] | w/ CT-ViT [47] |
| Optimizer | Adam [69] | Adam [69] | Adam [69] | Adam [69] |
| Learning rate - Visual Extractor | 0.0001 | 0.0001 | 0.00001 | 0.00001 |
| Learning rate - Classification Head(s) | 0.0001 | 0.0001 | 0.00001 | 0.00001 |
| Batch size | 4 | 4 | 4 | 4 |
| Epochs | 50 | 50 | 2 | 2 |
| Early stopping | ✓ | ✓ | ✓ | ✓ |

Table 3: Hyperparameters of the training for each model on the classification steps 1 and 2. For each configuration, we use the hyper-parameters that yield the best results. Early stopping is performed to obtain the checkpoint with the highest F1-Score on the validation set.

| | CT2Rep [10] | CT-AGRG |
|---|--------------|---------------|
| Optimizer | AdamW [70] | AdamW [70] |
| Learning rate - Visual Extractor | 0.00005 | - |
| Learning rate - Encoder Decoder | 0.00005 | 0.00005 |
| Weight decay | 0.01 | 0.01 |
| Batch size | 16 | 64 |
| Epochs | 100 | 100 |
| Early stopping | ✓ | ✓ |
| Tokenizer - Max. sequence length | 400 / report | 60 / sentence |
| Generation mode | Beam search | Beam search |
| Beam size | 4 | 4 |

Table 4: Hyperparameters of the training for each model on the generation step. For each configuration, we use the hyper-parameters that yield the best results. Early stopping is performed to obtain the checkpoint with the highest F1-Score on the validation set, triggered only after a minimum of 10 epochs to ensure sufficient training time and comparable iterations across experiments.

E. DATASET STATISTICS

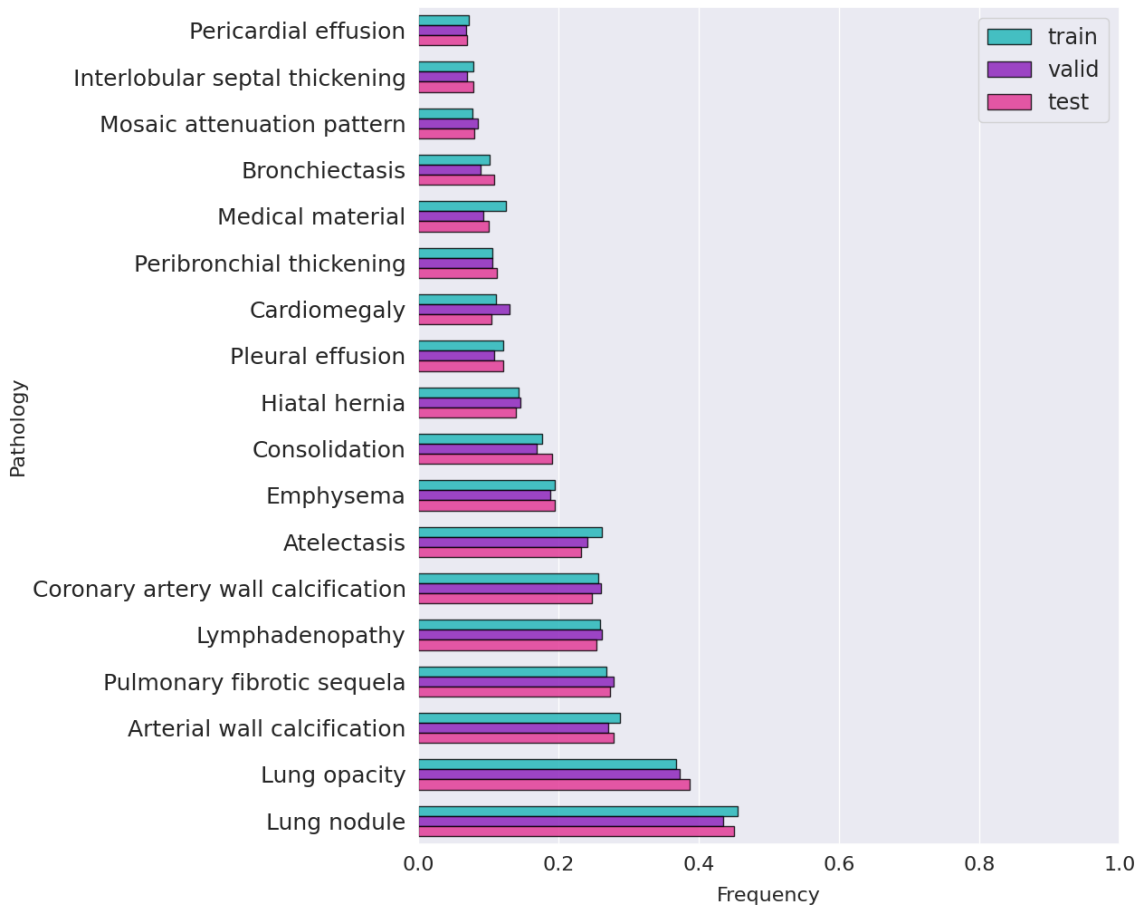


Fig. 4: Frequency of abnormalities in train, validation and test sets.

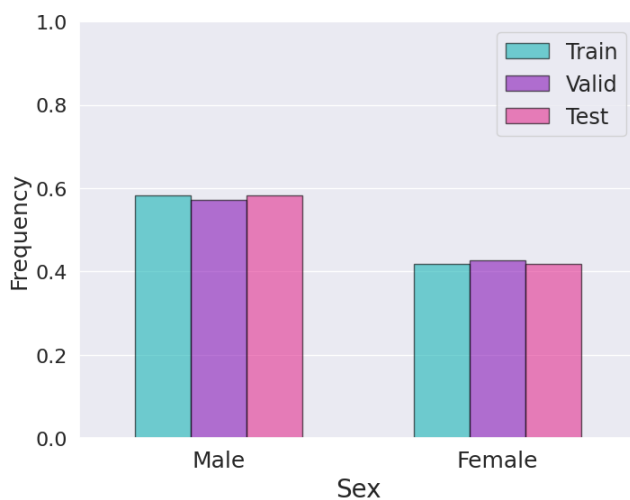


Fig. 5: Token count distribution per sentence from reports for train, validation and test sets.

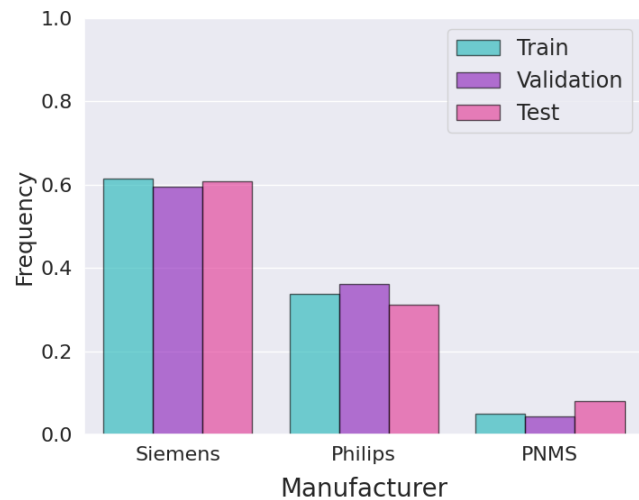


Fig. 6: Manufacturer distribution for train, validation and test sets.



Fig. 7: Age distribution for train, validation and test sets.

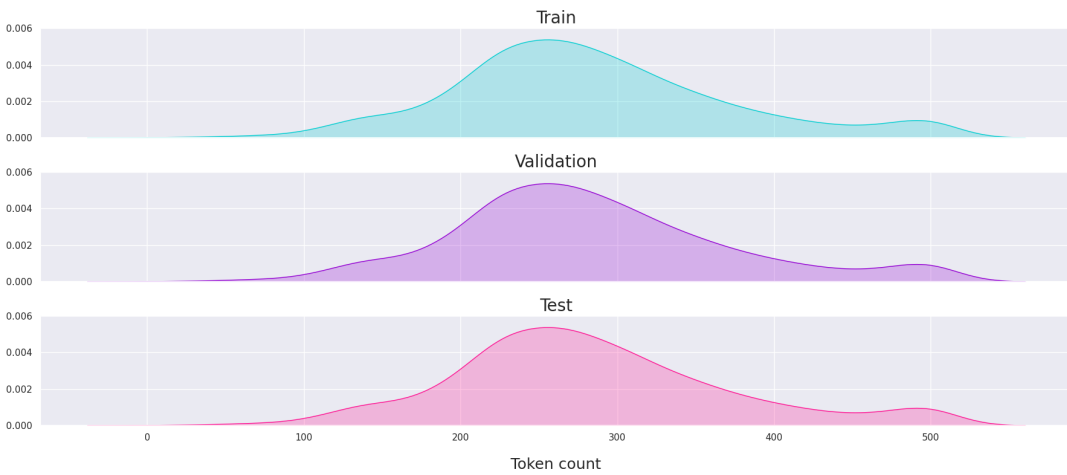


Fig. 8: Token count distribution from reports for train, validation and test sets.



Fig. 9: Token count distribution per sentence from reports for train, validation and test sets.